Speckle and fringe dynamics in imagingspeckle-pattern interferometry for spatial-filtering velocimetry

Jakobsen, Michael Linde; Iversen, Theis F. Q.; Yura, Harold T.; Hanson, Steen Grüner

Published in:
Applied Optics

Link to article, DOI:
10.1364/AO.50.005577

Publication date:
2011

Document Version
Publisher's PDF, also known as Version of record

Speckle and fringe dynamics in imaging-speckle-pattern interferometry for spatial-filtering velocimetry

Michael L. Jakobsen,[1,*] Theis F. Q. Iversen,[2] Harold T. Yura,[3] and Steen G. Hanson[1]

[1]DTU Fotonik, Department of Photonics Engineering, Technical University of Denmark, P.O. Box 49, DK-4000 Roskilde, Denmark

[2]OPDI Technologies A/S, Frederiksborgvej 399, 4000 Roskilde, Denmark

[3]Electronics and Photonics Laboratory, The Aerospace Corporation, P.O. Box 92957, Los Angeles, California 90009, USA

*Corresponding author: mlja@fotonik.dtu.dk

Received 2 May 2011; revised 19 August 2011; accepted 19 August 2011; posted 25 August 2011 (Doc. ID 146940); published 30 September 2011

This paper analyzes the dynamics of laser speckles and fringes, formed in an imaging-speckle-pattern interferometer with the purpose of sensing linear three-dimensional motion and out-of-plane components of rotation in real time, using optical spatial-filtering-velocimetry techniques. The ensemble-average definition of the cross-correlation function is applied to the intensity distributions, obtained in the observation plane at two positions of the object. The theoretical analysis provides a description for the dynamics of both the speckles and the fringes. The analysis reveals that both the magnitude and direction of all three linear displacement components of the object movement can be determined. Simultaneously, out-of-plane rotation of the object including the corresponding directions can be determined from the spatial gradient of the in-plane fringe motion throughout the observation plane. The theory is confirmed by experimental measurements.

OCIS codes: 030.6140, 120.6150, 120.6160, 070.6110, 100.2650.

1. Introduction

Speckle interferometry, combining an image of an object with an angularly offset reference wave, is a basic configuration for, e.g., electronic-speckle-pattern interferometry (ESPI) [1]. ESPI is a well-established nondestructive optical measurement technique used extensively to measure out-of-plane displacement fields of object deformations under load. Speckle photography [2] and digital speckle photography [3] are well-established and theoretically well-described [4] optical measurement techniques for measuring in-plane displacement fields of an imaged object during deformation or movement. Furthermore, these two techniques have been combined simultaneously to provide three-dimensional deformation field measurements of an object with a camera [5,6].

Considering rigid objects only, a design [7] for single-point measurements of three-dimensional motion of a rigid object has been proposed. This system is based on shearing of free-space-propagation speckle patterns for lateral movement and in-line Michelson interferometer for axial movement. However, this system will not differentiate between translation and rotation of the object. Therefore, a design [8], based on mixing a reference wave with a speckle field propagated through an imaging system, has been proposed. The reference and the speckle field mix under a well-defined angle, and spatial-filtering velocimetry [9,10] is applied to the image plane of the imaging-speckle interferometer. Therefore, three-dimensional motion of a rigid object has been extracted and measured from the image

0003-6935/11/285577-15$15.00/0

plane without being contaminated by a rotational motion of the object. This may potentially be performed in real time.

The in-line Michelson interferometer can be modified by angling the reference wave relative to the optical axis of the imaging system in order to implement the imaging-speckle-pattern interferometer [6]. The resulting phase will produce a regular fringe pattern in the image plane. This fringe pattern will translate through the image plane with a displacement/velocity that can be related directly to the out-of-plane displacement/velocity of the object. In contrast to previous studies, this configuration is designed for measuring out-of plane motion of a rigid object [8] with optical spatial-filtering velocimetry [10] having the center frequency of the spatial bandpass filter tuned to the fringe spacing. Spatial-filtering velocimetry can provide both the displacement/velocity and the direction of the fringe pattern in real time. With an adequately chosen point-spread function of the imaging system, and in case the object has an optically rough surface, speckles large enough to enclose the regular fringes will occur in the image of the illuminated part of the object. These speckles will translate in the image plane when the object performs an in-plane displacement or has an in-plane velocity component [4,7]. Again, optical spatial-filtering sensors, tuned to the mean speckle size, can monitor the speckle motion in two dimensions, and together with the optical spatial-filter monitoring the regular fringe pattern, full three-dimensional information of a rigid object's motion can be obtained simultaneously and in real time.

In case the object rotates in the object plane of an imaging system (speckle photography), the dynamics of the speckles will reveal no direct information about the angular velocity of the object. However, because there is a reference wave present in the observation plane, the phase or phase change of the individual speckles can be measured as, e.g., a local fringe movement or fringe velocity in the observation plane.

In order to theoretically describe the combined effects of both the fringe pattern and speckles in such a system, we consider the ensemble-average cross-correlation function of the intensity distributions in the image plane that is obtained for two positions of the object. The analytical expression will allow us to study the dynamics of the speckles and the fringes and their decorrelation lengths in response to object translation and rotation. Thus, the work presented here will address applications within the field of real-time, compact optical sensors and therefore pursue the possibilities of merging speckle interferometry and optical spatial-filtering velocimetry. The theoretical work is supported by experimental work.

2. Theory

The basic setup for describing the development and interaction of fields in the imaging-speckle-pattern interferometer is illustrated in Fig. 1. A rigid object with a rough surface at time t_1 is illuminated with a fundamental Gaussian (TEM_{00}) laser field, denoted as U_i. The in-plane coordinates of the object are denoted by the vector $\mathbf{r}_1 = (x, y)$, while the axial position is designated by the z coordinate, z_1. We define a rough surface as a surface having an rms surface roughness greater than the optical wavelength, and we illuminate a region on the object having a radius w_i that is large compared to any in-plane scale of the surface roughness. The optical field (U_s) scattered from the object surface is collected and propagated through an imaging system to be observed at the image plane where it is denoted as U_o. The optical axis of the imaging system is aligned with the z axis. The imaging system is described with a complex *ABCD* matrix [11] and has a limiting aperture in order to ensure that any scale of the surface roughness is unresolved in the image. Thus, fully developed speckles [12] will modulate the image of the illuminated object in the image plane. The image plane is positioned at a distance L from the object plane, and the intensity distribution in the image plane is designated by the two-dimensional vector, $\mathbf{p} = (p_x, p_y)$. A second fundamental Gaussian laser beam, incident in the image plane at an angle φ relative to the z axis, is added as a reference field, U_r. This angle can be decomposed into two orthogonal components, $\varphi = (\varphi_x, \varphi_y)$. At time t_2 the object is located at $\mathbf{r}_2$, where $\mathbf{r}_2 = \mathbf{r}_1 + \Delta\mathbf{r}$ and $z_2 = z_1 + \Delta z$.

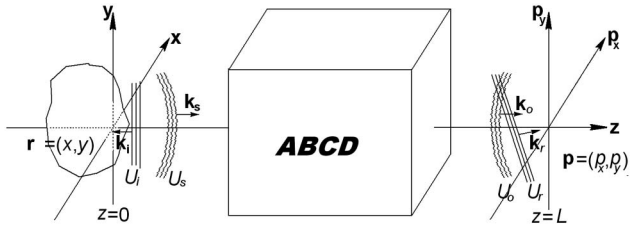

Fig. 1. Setup for describing the imaging-speckle-pattern interferometer.

For definiteness, we assume that the object is at rest at both t_1 and t_2 and that we have mixing between waves of equal optical wavelengths. Second, the description of the model will initially focus on linear displacement. Allowing the object to move with a constant velocity (v_x, v_y, v_z) within the time interval $\tau = t_2 - t_1$ creating a Doppler shift of the backscattered light will provide the same result. In this case, in the results presented below we can directly replace $\Delta\mathbf{r}$ by $\mathbf{v}\tau$ and Δz by $v_z\tau$, where $\mathbf{v} = (v_x, v_y)$ and v_z are in-plane and out-of-plane components of the object velocity, respectively. For simplicity, the angular motions of the object are restricted to out-of-plane angular displacements only. The out-of-plane angular displacements are described by $\boldsymbol{\theta} = (\theta_x, \theta_y)$ under the condition that $\boldsymbol{\omega} \cdot \mathbf{R} = 0$, where $\boldsymbol{\omega} = \mathbf{R} \times \boldsymbol{\theta}$ is the angular velocity of the object and $\mathbf{R}$ is the vector from the center of rotation to the center of the object plane. In this case, we can use the same model as specified for linear displacement by inserting a virtual

negative lens with a focal length of $f_o = -R/2$, where $R = |\mathbf{R}|$, and directly replace $\Delta\mathbf{r}$ with $R\Delta\boldsymbol{\theta}$ [13]. In the special case where the object is a cylinder, which rotates with respect to its axis of symmetry, R is the radius of the cylinder, $R\Delta\boldsymbol{\theta}$ is the peripheral displacement of the cylinder, and the virtual lens is a cylinder lens, oriented parallel to the axis of symmetry of the object.

We assume that both axial motion (Δz) and surface elevations ($\Delta z_e = w_i^2/R$) throughout the illuminated area of the object are small compared to both the depth of focus (d_o) of the imaging system and the confocal parameter ($2b$) of the illuminating beam: Δz, $\Delta z_e \ll d_o, 2b$. Hence, the illumination and the image configuration are not affected by the motion or the shape of the illuminated part of the object.

A. Ensemble-Average Cross-Correlation Function

For a stochastic process, the ensemble-average cross-correlation function of two intensity measurements, obtained at two positions in the observation plane due to light scattered from the object at time t_1 and t_2, can be expressed as [12]

$$\begin{aligned} C(\mathbf{p}_1, \mathbf{p}_2; \Delta\mathbf{r}, \Delta z) &= C(\mathbf{p}, \mathbf{p}+\mathbf{q}; \Delta\mathbf{r}, \Delta z) \\ &= \langle I(\mathbf{p}, t_1) I^*(\mathbf{p}-\mathbf{q}, t_2)\rangle, \end{aligned} \tag{1}$$

where the asterisk denotes the complex conjugate and angular brackets denote the ensemble average over the stochastic realization of the surface-height fluctuations of the rough surface. The two intensities $I(\mathbf{p}, t_1)$ and $I(\mathbf{p}-\mathbf{q}, t_2)$ denote the optical intensity (real) at the two positions $\mathbf{p}$ and $\mathbf{p}-\mathbf{q}$ in the image plane at the two time events considered above, respectively. The displacements, $\Delta\mathbf{r}$ and Δz, are linked to the two time events through the Green's function described in Eqs. (3) and (4).

In order to use the complex field amplitudes, $U_o(\cdot)$ and $U_r(\cdot)$, we assume that the polarization of the incident field is maintained during scattering and that the object and reference fields have identical polarizations in the image plane. Inserting the complex field amplitudes into Eq. (1) yields

$$\begin{aligned} C(\mathbf{p}, \mathbf{p}+\mathbf{q}; \Delta\mathbf{r}, \Delta z) = \langle &(U_o(\mathbf{p}, t_1) + U_r(\mathbf{p}))(U_o(\mathbf{p}, t_1) \\ &+ U_r(\mathbf{p}))^*(U_o(\mathbf{p}-\mathbf{q}, t_2) \\ &+ U_r(\mathbf{p}-\mathbf{q}))(U_o(\mathbf{p}-\mathbf{q}, t_2) \\ &+ U_r(\mathbf{p}-\mathbf{q}))^*\rangle \end{aligned} \tag{2}$$

The complex field amplitude of the reference field $U_r(\mathbf{p})$ is described locally at the image plane, while the complex field amplitude of the object field scattered off the object, $U_s(\mathbf{r}, t_i)$, is propagated to the observation plane via the Green's function, $G(\mathbf{r}, \mathbf{p}; z(t_i))$, to yield the corresponding image plane complex amplitude $U_o(\mathbf{p}, t_i)$. We have

$$U_o(\mathbf{p}, t_i) = \int_S \mathrm{d}^2\mathbf{r} U_s(\mathbf{r}, t_i) G(\mathbf{r}, \mathbf{p}, z(t_i)), \tag{3}$$

where the index ($i = 1, 2$) links t_i and z_i to the two object positions under consideration and where

$$\begin{aligned} G(\mathbf{r}, \mathbf{p}; z_i) = &-\frac{ik}{2\pi B}\exp(-ik(L' + z_i)) \\ &\times \exp\left(-\frac{ik}{2B}(A\mathbf{r}^2 - 2\mathbf{r}\cdot\mathbf{p} + D\mathbf{p}^2)\right) \end{aligned} \tag{4}$$

is the paraxial Green's function for propagation of a scalar field through an arbitrary paraxial optical system, described by the *ABCD* formalism [14]. The optical wavenumber is denoted by k, and L' describes the optical path length from object to observation. While L is the physical distance, L' is the optical propagation length through air and glass components. We assume an ideal clean imaging system with two lenses (of focal lengths f_1 and f_2) with a limiting Gaussian aperture located in the Fourier plane and having an e^{-1} transmission radius σ [11]. The assumption that the imaging system is unaffected by the object movement from time t_1 to t_2 ensures that the same *ABCD* elements can be used for both Green's functions. However, the initial ($L' + z_1$) and final ($L' + z_2$) optical path lengths must be inserted.

The complex field amplitude of the reflected field at the object plane is modeled as

$$U_s(\mathbf{r}, t) = U_i(\mathbf{r})\Psi(\mathbf{r}, t), \tag{5}$$

where $U_i(\mathbf{r})$ is the complex field amplitude (see Fig. 1) of light incident on the object and $\Psi(\mathbf{r}, t)$ is a complex reflection coefficient of zero mean, $\langle\Psi(\mathbf{r}, t)\rangle = 0$. However, the modulus of $\Psi(\mathbf{r}, t)$ is assumed to be constant and equal to unity (no absorption). The complex reflection coefficient models the spatial phase distortion of the scattered light as a stationary stochastic process. From time t to time $t + \tau$, the object moves as a rigid body by an amount of $\Delta\mathbf{r}(\tau)$ and accordingly $\Psi(\mathbf{r}, t)$ will change in time so that $\Psi(\mathbf{r} + \Delta\mathbf{r}(\tau), t + \tau) = \Psi(\mathbf{r}, t)$.

Following the analysis described in [13], the correlation function for the complex reflection coefficient is modeled by a Gaussian function and can be expressed as

$$\begin{aligned} B_\psi(\mathbf{r}_1, \mathbf{r}_2) &= \langle\Psi(\mathbf{r}_1, t_1)\Psi^*(\mathbf{r}_2, t_2)\rangle \\ &= \frac{4\pi}{k^2}\left(\frac{2}{\pi r_c^2}\exp\left[-\frac{2|\mathbf{r}_2 - \mathbf{r}_1|^2}{r_c^2}\right]\right), \end{aligned} \tag{6}$$

where r_c is a measure of the phase correlation length of the target surface. However, in the following we assume complete spatial incoherence (i.e., $r_c \to 0$) and find accordingly that Eq. (6) becomes

$$B_\Psi(\mathbf{r}_1, \mathbf{r}_2) = \left(\frac{4\pi}{k^2}\right)\delta(\mathbf{r}_2 - \mathbf{r}_1), \tag{7}$$

where $\delta(\cdot)$ is the Dirac delta function. This simplification holds for surfaces that appear matte at illumination. However, surfaces with, e.g., regular scratches or spatial coherent structures where $r_c \neq 0$ [13] or even $r_c \sim w_i$ do not fulfill the requirements for Eq. (7).

The spatial cross-correlation function given in Eq. (2) can be expanded and categorized into the following sum of product terms:

$$\begin{aligned} C(\mathbf{p},\mathbf{p}+\mathbf{q};\Delta\mathbf{r},\Delta z) = {} & C_{oooo}(\mathbf{p},\mathbf{p}+\mathbf{q};\Delta\mathbf{r},\Delta z) \\ & + C_{rrrr}(\mathbf{p},\mathbf{p}+\mathbf{q};\Delta\mathbf{r},\Delta z) \\ & + C_{oorr}(\mathbf{p},\mathbf{p}+\mathbf{q};\Delta\mathbf{r},\Delta z) \\ & + C_{oror}(\mathbf{p},\mathbf{p}+\mathbf{q};\Delta\mathbf{r},\Delta z) \\ & + C_{ooor}(\mathbf{p},\mathbf{p}+\mathbf{q};\Delta\mathbf{r},\Delta z) \\ & + C_{orrr}(\mathbf{p},\mathbf{p}+\mathbf{q};\Delta\mathbf{r},\Delta z), \end{aligned} \tag{8}$$

where the indices "o" and "r" reflect the various combinations of object and reference fields in the product terms. In [15] it has been shown that a scattering surface, which in a free-space-propagation system can produce fields with circular symmetric complex Gaussian and ergodic random variables, will produce fields of the same statistics in an imaging-configuration system. Therefore, the first term, containing the product of four scattered fields, can be expressed in terms of mutual second-order field correlations [12]:

$$\begin{aligned} & C_{oooo}(\mathbf{p},\mathbf{p}+\mathbf{q};\Delta\mathbf{r},\Delta z) \\ & \quad = |\langle U_o(\mathbf{p},t_1)U_o^*(\mathbf{p}-\mathbf{q},t_2)\rangle|^2 \\ & \qquad + \langle I_o(\mathbf{p},t_1)\rangle\langle I_o(\mathbf{p}-\mathbf{q},t_2)\rangle, \end{aligned} \tag{9}$$

where the intensity of the object field is denoted as $I_o(\cdot) = U_o(\cdot)U_o^*(\cdot)$. Inserting Eqs. (3) and (5) into Eq. (9) and changing the order of integration yields

$$\begin{aligned} & C_{oooo}(\mathbf{p},\mathbf{p}+\mathbf{q};\Delta\mathbf{r},\Delta z) \\ & \quad = \left| \iint_{S_r} \mathrm{d}^2\mathbf{r}_1\mathrm{d}^2\mathbf{r}_2[\langle \Psi(\mathbf{r}_1,t_1)\Psi^*(\mathbf{r}_2,t_2)\rangle \right. \\ & \qquad \left. \times U_i(\mathbf{r}_1)G(\mathbf{r}_1,\mathbf{p},z_1)U_i^*(\mathbf{r}_2)G^*(\mathbf{r}_2,\mathbf{p}-\mathbf{q},z_2)] \right|^2 \\ & \qquad + \iint_{S_r} \mathrm{d}^2\mathbf{r}_1\mathrm{d}^2\mathbf{r}_1'[\langle \Psi(\mathbf{r}_1,t_1)\Psi^*(\mathbf{r}_1',t_1)\rangle \\ & \qquad \times U_i(\mathbf{r}_1)G(\mathbf{r}_1,\mathbf{p},z_1)U_i^*(\mathbf{r}_1')G^*(\mathbf{r}_1',\mathbf{p},z_1)] \\ & \qquad \times \iint_{S_r} \mathrm{d}^2\mathbf{r}_2\mathrm{d}^2\mathbf{r}_2'[\langle \Psi(\mathbf{r}_2,t_2)\Psi^*(\mathbf{r}_2',t_2)\rangle \\ & \qquad \times U_i(\mathbf{r}_2)G(\mathbf{r}_2,\mathbf{p}-\mathbf{q},z_2)U_i^*(\mathbf{r}_2') \\ & \qquad \times G^*(\mathbf{r}_2',\mathbf{p}-\mathbf{q},z_2)]. \end{aligned} \tag{10}$$

As we assume complete spatial incoherence (i.e., $r_c \to 0$), Eq. (7) dictates that the only nonzero contribution to the integration is obtained for $\mathbf{r}_2 = \mathbf{r}_1 + \Delta\mathbf{r}$, where $\Delta\mathbf{r}$ is the in-plane displacement of the object from t_1 to t_2. Thus, we obtain

$$\begin{aligned} & C_{oooo}(\mathbf{p},\mathbf{p}+\mathbf{q};\Delta\mathbf{r},\Delta z) \\ & \quad = \left(\frac{4\pi}{k^2}\right)^2 \left| \int_{-\infty}^{\infty} \mathrm{d}^2\mathbf{r} U_i(\mathbf{r})G(\mathbf{r},\mathbf{p},z_1)U_i^*(\mathbf{r}+\Delta\mathbf{r})G^*(\mathbf{r} \right. \\ & \qquad \left. + \Delta\mathbf{r},\mathbf{p}-\mathbf{q},z_1+\Delta z) \right|^2 \\ & \qquad + \int_{-\infty}^{\infty} \mathrm{d}\mathbf{r} I_i(\mathbf{r})G(\mathbf{r},\mathbf{p},z_1)G^*(\mathbf{r},\mathbf{p},z_1) \\ & \qquad \times \int_{-\infty}^{\infty} \mathrm{d}\mathbf{r} I_i(\mathbf{r}+\Delta\mathbf{r})G(\mathbf{r}+\Delta\mathbf{r},\mathbf{p}-\mathbf{q},z_2)G^*(\mathbf{r} \\ & \qquad + \Delta\mathbf{r},\mathbf{p}-\mathbf{q},z_2). \end{aligned} \tag{11}$$

The reference wave field is independent of the ensemble of surfaces and the position of the object; thus, the term containing the product of four reference fields is deterministic, i.e.,

$$C_{rrrr}(\mathbf{p},\mathbf{p}+\mathbf{q};\Delta\mathbf{r},\Delta z) = I_r(\mathbf{p})I_r(\mathbf{p}-\mathbf{q}), \tag{12}$$

where the intensity of the reference wave is denoted as $I_r(\cdot) = U_r(\cdot)U_r^*(\cdot)$. The four terms of the spatial cross-correlation function, containing products of two object fields and two reference fields, have been divided into the following two groups:

$$\begin{aligned} & C_{oror}(\mathbf{p},\mathbf{p}+\mathbf{q};\Delta\mathbf{r},\Delta z) \\ & \quad = U_r^*(\mathbf{p})U_r^*(\mathbf{p}-\mathbf{q})\langle U_o(\mathbf{p},t_1)U_o(\mathbf{p}-\mathbf{q},t_2)\rangle + cc \\ & \qquad + U_r^*(\mathbf{p})U_r(\mathbf{p}-\mathbf{q})\langle U_o(\mathbf{p},t_1) \\ & \qquad \times U_o^*(\mathbf{p}-\mathbf{q},t_2)\rangle + cc, \end{aligned} \tag{13}$$

$$\begin{aligned} C_{oorr}(\mathbf{p},\mathbf{p}+\mathbf{q};\Delta\mathbf{r},\Delta z) = {} & I_r(\mathbf{p}-\mathbf{q})\langle I_o(\mathbf{p},t_1)\rangle \\ & + I_r(\mathbf{p})\langle I_o(\mathbf{p}-\mathbf{q},t_2)\rangle. \end{aligned} \tag{14}$$

The first term of $C_{oror}(\mathbf{p},\mathbf{p}+\mathbf{q};\Delta\mathbf{r},\Delta z)$ on the right-hand side of Eq. (13) is a product of fields, where the individual fields do not appear together with their corresponding complex conjugate fields, and thus the product becomes equal to zero upon integration. For the second term of $C_{oror}(\mathbf{p},\mathbf{p}+\mathbf{q};\Delta\mathbf{r},\Delta z)$ and its complex conjugate, we substitute Eqs. (3) and (5) into the expression, change the order of integration, use Eq. (7), and obtain

$$\begin{aligned} & C_{oror}(\mathbf{p},\mathbf{p}+\mathbf{q};\Delta\mathbf{r},\Delta z) \\ & \quad = \left(\frac{4\pi}{k^2}\right) U_r^*(\mathbf{p})U_r(\mathbf{p}-\mathbf{q}) \int_{-\infty}^{\infty} \mathrm{d}^2\mathbf{r} U_i(\mathbf{r})G(\mathbf{r},\mathbf{p},z_1) \\ & \qquad \times U_i^*(\mathbf{r}+\Delta\mathbf{r})G^*(\mathbf{r}+\Delta\mathbf{r},\mathbf{p}-\mathbf{q},z_1+\Delta z) \\ & \qquad + cc. \end{aligned} \tag{15}$$

Again, substituting Eqs. (3) and (5) into Eq. (14), changing the order of integration, and using Eq. (7), we obtain

$$C_{oorr}(\mathbf{p},\mathbf{p}+\mathbf{q};\Delta\mathbf{r},\Delta z)$$
$$= \left(\frac{4\pi}{k^2}\right) I_r(\mathbf{p}-\mathbf{q}) \int_{-\infty}^{\infty} \mathrm{d}^2\mathbf{r} I_i(\mathbf{r}) G(\mathbf{r},\mathbf{p},z_1) G^*(\mathbf{r},\mathbf{p},z_1)$$
$$+ \left(\frac{4\pi}{k^2}\right) I_r(\mathbf{p}) \int_{-\infty}^{\infty} \mathrm{d}^2\mathbf{r} I_i(\mathbf{r}+\Delta\mathbf{r})$$
$$\times G(\mathbf{r}+\Delta\mathbf{r},\mathbf{p}-\mathbf{q},z_2) G^*(\mathbf{r}+\Delta\mathbf{r},\mathbf{p}-\mathbf{q},z_2). \quad (16)$$

Further, all product combinations containing only a single object or reference field become zero upon integration.

The optical field incident on the object surface is assumed to be a plane wave with a Gaussian distributed field propagating along the optical axis of the system:

$$U_i(\mathbf{r}) = E_i \exp\left(-\frac{|\mathbf{r}|^2}{w_i^2}\right), \quad (17)$$

where the phase in the object plane is assumed equal to zero. At the object surface (at $z = 0$), the amplitude of the field is E_i, and the profile radius is w_i. The optical reference field incident at the observation plane is also a plane wave with a Gaussian distributed field:

$$U_r(\mathbf{p}) = E_r \exp\left(-\frac{|\mathbf{p}|^2}{w_r^2} + ik\varphi\cdot\mathbf{p}\right). \quad (18)$$

The phase of the field is set equal to zero at the origin of the observation plane. At the observation plane, the amplitude of the reference field is E_r, and the profile radius is w_r.

1. *Speckle and Fringe Dynamics for a Linearly Displaced Object*

In order to measure linear translation of the object, we insert into Eq. (4) the *ABCD* matrix elements, specifying a clean imaging system: $A = -f_2/f_1$, $B = -2if_1f_2/(k\sigma^2)$, $D = -f_1/f_2$. Then, inserting z_1, z_2, Eqs. (4), (17), and (18) into Eqs. (11), (12), (15), and (16) and carrying out the resulting Gaussian integrations, we find the following nonzero correlation terms. Specifically, for the object fields only we find

$$C_{oooo}(\mathbf{p},\mathbf{p}+\mathbf{q};\Delta\mathbf{r},\Delta z)$$
$$= \frac{16E_i^4}{k^4\rho^4\left(1+\frac{f_1^2}{f_2^2}\frac{\rho^2}{2w_i^2}\right)^2} \times \exp\left(-\frac{2||\mathbf{p}|^2+|\mathbf{p}+\mathbf{q}|^2|}{\frac{\rho^2}{2}+\frac{f_2^2}{f_1^2}w_i^2}\right)$$
$$\times \left(1+\exp\left(-\frac{2\left|\mathbf{q}+\left(\frac{f_2}{f_1}+\frac{4f_1f_2}{k^2\sigma^2w_i^2}\right)\Delta\mathbf{r}\right|^2}{\rho^2\left(1+\frac{4f_1^2}{k^2\sigma^2w_i^2}\right)}\right)\right), \quad (19a)$$

where $\rho = 2\sqrt{2}f_2/(k\sigma)$ is the mean e^{-2} speckle radius. As in [13], the last exponential function in Eq. (19a) describes the speckle translation due to in-plane displacement of the object, while the first exponential function depicts the relation between the image intensity and the correlation function. The peak value of the correlation function depends on the image intensity via the positions of the two points to be correlated ($\mathbf{p}$ and $\mathbf{p}+\mathbf{q}$). The corresponding contribution, for the reference fields only, is given as

$$C_{rrrr}(\mathbf{p},\mathbf{p}+\mathbf{q};\Delta\mathbf{r},\Delta z)$$
$$= E_r^4 \exp\left(-\frac{2(|\mathbf{p}|^2+|\mathbf{p}+\mathbf{q}|^2)}{w_r^2}\right). \quad (19b)$$

Further, the cross terms $C_{oorr}(\mathbf{p},\mathbf{p}+\mathbf{q};\Delta\mathbf{r},\Delta z)$ and $C_{oror}(\mathbf{p},\mathbf{p}+\mathbf{q};\Delta\mathbf{r},\Delta z)$ are given as

$$C_{oorr}(\mathbf{p},\mathbf{p}+\mathbf{q};\Delta\mathbf{r},\Delta z)$$
$$= \frac{4E_i^2E_r^2}{k^2\rho^2\left(1+\frac{f_1^2}{f_2^2}\frac{\rho^2}{2w_i^2}\right)^2} \times \exp\left(-\left(\frac{2}{w_r^2}+\frac{2}{\frac{\rho^2}{2}+\frac{f_2^2}{f_1^2}w_i^2}\right)\right.$$
$$\left.\times|\mathbf{p}|^2\right) \times \left(\exp\left(-\frac{2}{w_r^2}(2\mathbf{p}\cdot\mathbf{q}+|\mathbf{q}|^2)\right)\right.$$
$$\left.+\exp\left(-\frac{2(2\mathbf{p}\cdot\mathbf{q}+|\mathbf{q}|^2)}{\frac{\rho^2}{2}+\frac{f_2^2}{f_1^2}w_i^2}\right)\right), \quad (19c)$$

$$C_{oror}(\mathbf{p},\mathbf{p}+\mathbf{q};\Delta\mathbf{r},\Delta z)$$
$$= \frac{4E_i^2E_r^2}{k^2\rho^2\left(1+\frac{f_1^2}{f_2^2}\frac{\rho^2}{2w_i^2}\right)} \times \cos(k(2\Delta z+\varphi\cdot\mathbf{q}))$$
$$\times \exp\left(-\frac{\left|\mathbf{q}+\left(\frac{f_2^2}{f_1^2}+\frac{4f_1f_2}{k^2\sigma^2w_i^2}\right)\Delta\mathbf{r}\right|^2}{\rho^2\left(1+\frac{4f_1^2}{k^2\sigma^2w_i^2}\right)}\right)$$
$$\times \exp\left(-\left(\frac{1}{w_r^2}+\frac{1}{\frac{\rho^2}{2}+\frac{f_2^2}{f_1^2}w_i^2}\right)\right.$$
$$\left.\times(|\mathbf{p}|^2+|\mathbf{p}+\mathbf{q}|^2)\right). \quad (19d)$$

Equations (19b) and (19c) are independent of the displacement $\Delta\mathbf{r}$ and therefore of no interest for the present discussion. The speckle dynamics in Eq. (19d) is similar to Eq. (19a), except for the influence of the width of the reference beam w_r in the image-intensity-related correlation term. However, the additional cosine function describes a uniform fringe structure modulating the speckles with a fringe spacing ($\Lambda_{fr} = \lambda/|\varphi|$) and fringe orientation defined by the angle (φ) between the object and reference waves. Moreover, the fringes will shift uniformly in the

observation plane as the object is displaced out of plane, and the fringes will move in a direction that depends on the direction of the out-of-plane motion of the object.

The individual speckles define areas of coherence and constructive interference in the observation plane. Therefore, the phases of the fringe patterns in different speckles are completely uncorrelated. Further, as the speckles decorrelate, the fringes will decorrelate as well.

2. *Speckle and Fringe Dynamics for an Angular Displaced Object*

In order to measure angular velocity, we insert into Eq. (4) the *ABCD* matrix elements, specifying a clean imaging system with the virtual lens emulating the angle of rotation located in the object plane: $A = -f_2/f_1 - 4if_1f_2/(Rk\sigma^2)$, $B = -2if_1f_2/(k\sigma^2)$, $D = -f_1/f_2$. We replace $\Delta\mathbf{r}$ with $R\Delta\boldsymbol{\theta}$ and insert z_1, z_2, Eqs. (4), (17), and (18) into Eqs. (11), (12), (15), and (16) and carry out the resulting Gaussian integrations. Finally, we find the following two correlation terms, which have been changed due to introducing the virtual lens:

$$C_{oooo}(\mathbf{p}, \mathbf{p}+\mathbf{q}; \Delta\theta, \Delta z) = \frac{16E_i^4}{k^4\rho^4\left(1+\frac{f_1^2}{f_2^2}\frac{\rho^2}{2w_i^2}\right)^2} \times \exp\left(-\frac{2[|\mathbf{p}|^2+|\mathbf{p}+\mathbf{q}|^2]}{\frac{\rho^2}{2}+\frac{f_2^2}{f_1^2}w_i^2}\right) \times \left(1+\exp\left(-\frac{2|\Delta\boldsymbol{\theta}|^2}{\frac{4}{k^2w_i^2}+\frac{\sigma^2}{f_1^2}}\right) \times \exp\left(-\frac{2\left|\mathbf{q}+\left(\frac{f_2}{f_1}+\frac{4f_1f_2}{k^2\sigma^2w_i^2}\right)R\Delta\boldsymbol{\theta}\right|^2}{\rho^2\left(1+\frac{4f_1^2}{k^2\sigma^2w_i^2}\right)}\right)\right). \quad (20a)$$

Again, the first exponential function describes the image-intensity-related correlation term. The second exponential function describes the decorrelation of the speckle pattern. The last exponential function in Eq. (20a) describes the speckle translation due to out-of-plane rotation of the object. However, in accordance with the literature [13], the speckle dynamics does not measure the angular velocity; it merely measures the peripheral velocity of the object, which is proportional to R.

The decorrelation arises as the object rotates and as the corresponding objective speckles, to be observed in front of the imaging system, rotate as a three-dimensional (3D) structure. As a 3D speckle structure rotates $|\Delta\boldsymbol{\theta}|$ through the numerical aperture (σ/f_1) at the entrance of the imaging system, including a diffractive contribution $[2/(kw_i)]$, the speckle pattern observed in the image plane changes gradually. As a 3D structure sweeps through the entire numerical aperture, the speckle pattern decorrelates completely.

Specifically, when comparing the decorrelation term with the minimum measurable angular displacement $(\Delta\theta_{\min})$, defined as the angular shift that shifts the speckle pattern by a single speckle radius $\Delta\theta_{\min} = \rho/R$, we find $R^2 = d_o^2$, where the focal depth (d_o) is defined as $4f_1^2/(k\sigma^2)$. In case of $R \ll d_o^2$, the decorrelation of the speckle patterns due to object rotation will be so severe that the speckle correlation cannot resolve any speckle shift due to the peripheral velocity. Therefore, any measured shift in the speckle pattern is caused by linear in-plane translation of the object.

The cross term $C_{ooor}(\mathbf{p}, \mathbf{p}+\mathbf{q}; \Delta\boldsymbol{\theta}, \Delta z)$ is given as

$$C_{ooor}(\mathbf{p}, \mathbf{p}+\mathbf{q}; \Delta\boldsymbol{\theta}, \Delta z) = \frac{4E_i^2E_r^2}{k^2\rho^2\left(1+\frac{f_1^2}{f_2^2}\frac{\rho^2}{2w_i^2}\right)} \cos\left(k(2\Delta z + \varphi\cdot\mathbf{q}) + \frac{k(2\mathbf{p}+\mathbf{q})\cdot\Delta\boldsymbol{\theta}}{\frac{f_2}{f_1}+\frac{\rho^2}{2w_i^2}}\right) \times \exp\left(-\frac{\left|\mathbf{q}+\left(\frac{f_2^2}{f_1^2}+\frac{4f_1f_2}{k^2\sigma^2w_i^2}\right)R\Delta\boldsymbol{\theta}\right|^2}{\rho^2\left(1+\frac{4f_1^2}{k^2\sigma^2w_i^2}\right)}\right) \times \exp\left(-\left(\frac{1}{w_r^2}-\frac{1}{\frac{\rho^2}{2}+\frac{f_2^2}{f_1^2}w_i^2}\right) \times (|\mathbf{p}|^2+|\mathbf{p}+\mathbf{q}|^2) - \frac{2|\Delta\boldsymbol{\theta}|^2}{\frac{4}{k^2w_i^2}+\frac{\sigma^2}{f_1^2}}\right). \quad (20b)$$

The speckle dynamics in Eq. (20b) is equivalent to Eq. (20a) except for the influence of the width of the reference beam w_r in the image-intensity-related correlation term. However, the cosine function, describing the fringe structure, now contains a second term, which dictates a phase shift with a spatial gradient with regard to $\mathbf{p}$ and as a function of the angular velocity $\Delta\boldsymbol{\theta}$—not the peripheral velocity.

For a more detailed discussion, we assume that the plane of incidence is parallel with the xz plane, $\varphi = (\varphi_x, 0)$, $|M| = |f_2/f_1| \gg \sigma/(2w_i)$, $Mw_i = w_r$ and that $|\varphi_x| \gg |\Delta\theta_x/M|$. This means that the fringe intensity varies along the x axis. In Fig. 2, the corresponding correlation function illustrates the main contributions: the Gaussian background with an e^{-2} radius of Mw_i is the sum of the individual correlation functions of the image of the illuminated region on the object [Eq. (20a)], the reference beam [Eq. (19b)], and the corresponding cross terms [Eq. (19c)]. The oscillations are due to the correlation function of the fringe patterns [Eq. (20b)]. In this

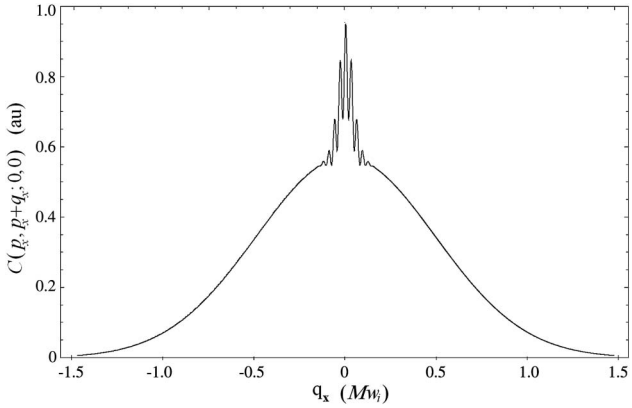

Fig. 2. Ensemble-averaged correlation function plotted versus q_x in units of Mw_i.

case, the mean speckle contains $2\rho\varphi_x/\lambda = 4.5$ fringes. The Gaussian pedestal located just underneath the oscillations, having a radius of $0.1 \times Mw_i$, is the correlation function of the speckles [Eq. (20a)]. The dynamics of the fringes are described as the displacement in the correlation plane of a given phase of the cosine function. Thus, the corresponding relation between q_x, Δz, and $\Delta\theta$ is obtained by requiring that the argument of the cosine function is kept at a constant value during the time interval from t_1 to t_2.

In case the object undergoes an out-of-plane rotation with respect to the y axis, $\Delta\boldsymbol{\theta} = (\Delta\theta_x, 0)$, we find that the fringe patterns move along the p_x direction, according to

$$q_x = -\frac{2}{\varphi_x}\left(\Delta z + \frac{\Delta\theta_x p_x}{M}\right), \tag{21}$$

while the fringe patterns carry out no displacement along the p_y direction. The response of the fringe motion q_x to object rotation $\Delta\theta_x$ is independent of R and increases linearly with the distance p_x. Within the criterion of $|\varphi_x| \gg |\Delta\theta_x/M|$, the fringe spacing is constant throughout the entire image. As discussed after Eq. (20b), the decorrelation term restricts the maximum angular displacement ($\Delta\theta_x$) to the numerical aperture (σ/f_1) at the entrance of the imaging system. Thus, as the speckle size relates to the same numerical aperture given the magnification (f_2/f_1), speckles will decorrelate during the angular displacement in case the variations in fringe displacement throughout the individual speckles become comparable with half the fringe spacing. Measuring the displacement of the fringes at two arbitrary positions in the observation plane, though with a mutual distance of d_p, the angular displacement $\Delta\theta_x$ can be found independent of Δz and the center of rotation:

$$\Delta\theta_x = \frac{\varphi_x M}{2d_p}(q_{x2} - q_{x1}), \tag{22}$$

In case the object moves simultaneously along the z axis and the center of rotation is unknown, the actual p_x position of the center of rotation must be determined in order to measure the correct value of Δz. This issue is discussed in more detail in Section 4. The fringe spacing is uniform throughout the observation plane and defined by $\Lambda_{\mathrm{fr}} = \lambda/\varphi_x$. However, in case the criterion of $|\varphi_x| \gg |\Delta\theta_x/M|$ is not fulfilled, there will be a minor change to the fringe spacing, which depends on the angular displacement. Accordingly, the fringe spacing will be $\Lambda_{\mathrm{fr}} = \lambda/(\varphi_x + \Delta\theta/M)$.

In case the object carries out an out-of-plane rotation with respect to the x axis, $\Delta\boldsymbol{\theta} = (0, \Delta\theta_y)$, the fringe intensity will still vary uniformly along the p_x axis. Again, the fringe patterns move in the p_x direction, while now there is a gradient in fringe movement with respect to the p_y position:

$$q_x = -\frac{2\Delta\theta_y}{\varphi_x M}p_y. \tag{23}$$

The response of the fringe motion q_x to object rotation $\Delta\theta_y$ is independent of R and increases linearly with the distance p_y. Again, the variation in fringe displacement along the y axis throughout a speckle is restricted by the speckle decorrelation. Further, the displacement of the fringes can be measured at two arbitrary positions in the observation plane, though with a mutual distance of d_p, and the angular displacement $\Delta\theta_y$ can be found as

$$\Delta\theta_y = \frac{\varphi_x M}{2d_p}(q_{y2} - q_{y1}). \tag{24}$$

In case the object moves simultaneously along the z axis and the center of rotation is unknown, the actual y position of the center of rotation must be determined in order to measure the correct value of Δz. More details can be found in Section 4.

B. Optical Spatial-Filtering Velocimetry

The technology of optical spatial-filter velocimetry [10] is applied to the intensity distribution in the observation plane in order to extract and track any movement of the speckles and the fringes individually and instantaneously. However, it is necessary to distinguish between speckle correlation and optical spatial filtering. Doing speckle correlation as described in Subsection 2.A, a spatial displacement of $\mathbf{q}$ of an intensity structure during two image acquisitions is measured. Applying optical spatial-filtering velocimetry, an intensity variation is obtained as a selected spatial frequency component in the intensity distribution travels across the filter located at a fixed position in the observation plane ($\mathbf{q} = 0$). In the same limit as Eq. (21), the phase shift $\Delta\phi$ of the cosine function can be written as

$$\Delta\phi(\Delta\theta_x) = 2k\left(\Delta z + \frac{\Delta\theta_x p_x}{M}\right). \tag{25}$$

Therefore, in the limit of $|\varphi_x| \gg |\Delta\theta_x/M|$, the two measurement techniques differ only by a proportionality factor given as $q_x/\Delta\varphi = \Lambda_{\mathrm{fr}}/(2\pi)$. In the limit of

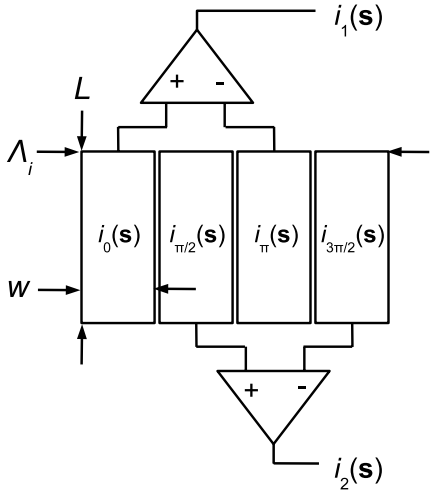

Fig. 3. Four detectors define a single unit cell from a spatial bandpass filter with N unit cells. The four detectors provide two differential signals with a phase lag of $\pi/2$.

$|\varphi_x| \sim |\Delta\theta_x/M|$, the proportionality factor deviates with the angular displacement dependent term; however, with regard to the signal-phase shift, Eq. (25) still holds because $q_x = 0$. In case we measure motion $(\Delta q_x/\Delta t)$ of the fringes rather than displacement and signal frequency $(2\pi f_s = \Delta\phi/\Delta t)$ rather than signal-phase shift, we have

$$f_s = \frac{2}{\lambda}\left(v_z + \frac{\Delta\theta_x p_x}{\Delta t\, M}\right) = \frac{1}{\Lambda_{\mathrm{fr}}}\frac{\Delta q_x}{\Delta t}. \tag{26}$$

Therefore, in the following we assume that the fringe spacing $\Lambda_{\mathrm{fr}} = \lambda/\varphi_x$ is a well-calibrated constant.

In principle, a filter dedicated for optical spatial-filtering velocimetry responds to the presence of a narrow spatial frequency component and produces one or several photocurrents $i_\theta(\mathbf{s})$ at mutually different phase steps, indicated by the index, θ. Say that the addressed optical structure shifts along the p_x axis of the observation plane by a distance of s_x according to object movement: then the photocurrents oscillate through a phase change proportional to s_x. The response of such a photocurrent $i_\theta(\mathbf{s})$ can be described as a function of the displacement $\mathbf{s}$ of the addressed optical structure relative to the spatial filter:

$$i_\theta(\mathbf{s}) = \int_{-\infty}^{\infty} \mathrm{d}^2\mathbf{p} I(\mathbf{p}-\mathbf{s}) h_\theta(\mathbf{p}). \tag{27}$$

The response function of the spatial filter is $h_\theta(\mathbf{s})$, where $\mathbf{s}$ might be a function of time. With infinite integration limits, we let the response function or the image intensity define the physical size of the spatial filter. The spatial power spectrum of the photocurrent is given by $P_i(\xi) = P_1(\xi)H(\xi)$, where $P_I(\xi)$ is the spatial power spectrum of the optical intensity distribution, $I(\mathbf{p})$, and $H(\xi)$ is the spatial power spectrum of the transmission function.

An optical spatial filter with a rectangular-weighted, linear rectangular-array transmission function [16] can be implemented as a comb array consisting of N equally weighted unit cells. The spacing between the unit cells in the array is labeled as Λ_i, where the index $(i = x, y, z)$ indicates the component of displacement to be measured. The number (N) of unit cells and the spacing (Λ_i) between the unit cells determines the selectivity and the spatial center frequency of the filter, respectively. The unit cell contains four rectangular photodetectors with dimensions of $w \times L = (\Lambda_i/4) \times L$, having rectangular transmission functions. The corresponding unit cell, illustrated in Fig. 3, produces two differential photocurrents, having a phase lag of $\pi/2$. The differential photocurrents are $i_1(\mathbf{s}) = i_0(\mathbf{s}) - i_\pi(\mathbf{s})$ and $i_2(\mathbf{s}) = i_{\pi/2}(\mathbf{s}) - i_{3\pi/2}(\mathbf{s})$.

The corresponding spatial power spectrum $H(\xi)$ for the transmission function [16] of the spatial filter producing each of the differential photocurrents becomes

$$H(\xi) = (2\xi_0 N\Lambda_i w)^2 \left\{ \sum_{n=-\infty}^{\infty} \delta(\xi - (2n+1)\xi_0) \times \mathrm{sinc}^2(w\xi) \right\} \otimes \mathrm{sinc}^2(N\Lambda_i \xi), \tag{28}$$

where N is the number of unit cells within the truncated transmission function (i.e., the length of the spatial filter is $N\Lambda_i$), $\xi_0 = 1/\Lambda_i$ is the fundamental spatial frequency of the filter, and $\otimes$ indicates convolution. Equation (28) considers one dimension only; thus, the influence of height L of the unit cell is not included. The power spectrum is plotted for $N = 9$, 65, and 3 in Figs. 4–6, respectively. The power spectrum contains no information about the individual phases of the spatial filter; thus Eq. (28) is identical for both parts of the spatial filter producing the

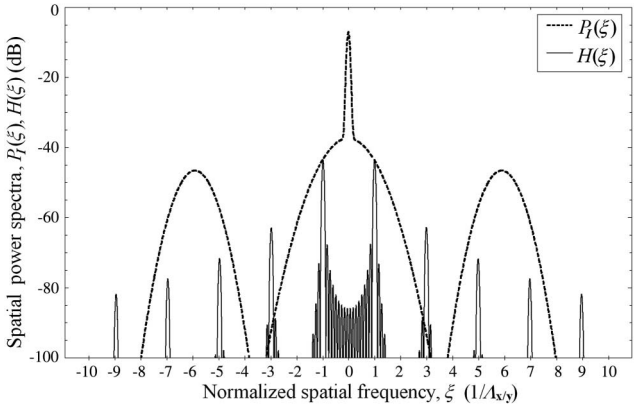

Fig. 4. Spatial power spectrum [Eq. (28)] of a spatial filter designed to respond to the presence of speckles. The spatial filter is designed with a moderate selectivity, defined by $N = 9$ unit cells in the array. The unit of the spatial frequency is $1/\Lambda_{x/y}$. The fundamental frequency of the spatial filter is designed to coincide with the spectral content of the speckles (dashed line). The logarithmic scales for the two power spectra are equivalent. However, the absolute magnitudes are arbitrary.

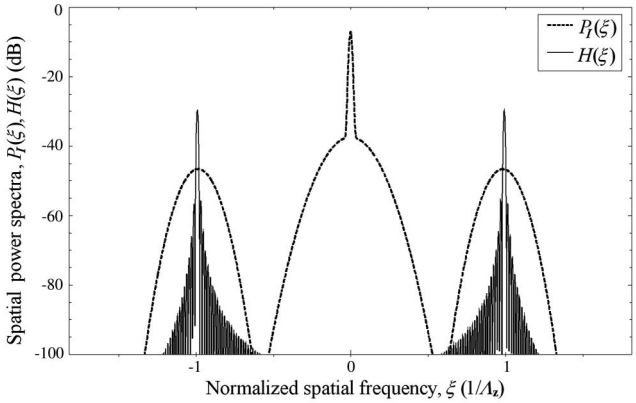

Fig. 5. Spatial power spectrum [Eq. (28)] of a spatial filter designed to respond to the presence of fringes. The spatial filter is designed with a high selectivity, defined by $N = 65$ unit cells in the array. The unit of the spatial frequency is $1/\Lambda_z$. The fundamental frequency of the spatial filter is designed to coincide with the spectral content of the fringe patterns (dashed line). The logarithmic scales for the two power spectra are equivalent. However, their absolute magnitudes are arbitrary.

two differential signals, $i_1(\mathbf{s})$ and $i_2(\mathbf{s})$. Alternatively, the two differential photocurrents with a phase lag of $\pi/2$ can be implemented with three detectors [17], and optical spatial filters with better suppression of all the harmonics can be found in, e.g., [10].

In case of linear translation of the object in 3D, Eqs. (19a) and (19d) predict that the fringe spacing is uniform throughout the observation plane and that the displacement of the fringes or the speckles in response to object motion is uniform as well. Therefore, an optical spatial filter with a relatively high selectivity ($N = 8$–100) applied to this type of fringe and speckle dynamics can provide measurements with high accuracy. The selectivity increases with the number of unit cells in the array [10]. Nevertheless, the maximum selectivity of the photocurrent

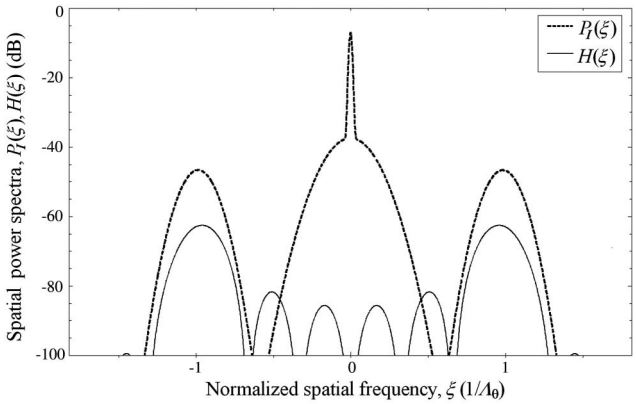

Fig. 6. Spatial power spectrum [Eq. (28)] of a spatial filter designed to respond to the presence of fringes. The spatial filter is designed with a very low selectivity, defined by $N = 3$ unit cells in the array. The unit of the spatial frequency is $1/\Lambda_{x/y}$. The fundamental frequency of the spatial filter is designed to coincide with the spectral content of the fringe patterns (dashed line); see Eq. (30). The logarithmic scales for the two power spectra are equivalent. However, their absolute magnitudes are arbitrary.

is limited by the decorrelation length of the speckles. The ensemble-average power spectrum of the intensity distribution $P_I(\boldsymbol{\xi})$ can be determined as the inverse Fourier transform of the autocorrelation function in Fig. 2 and is illustrated as the solid line in Fig. 4. The narrow Gaussian contribution at the top and centered at $\xi = 0$ consists of the spectra of the image of the illumination spot and the reference beam. The broad Gaussian contribution below and centered at $\xi = 0$ is the speckle spectrum, and the two satellite peaks centered at $\xi = \pm 6$ arise from the fringe pattern. Further, the dashed line in Fig. 4 illustrates the power spectrum, $H(\boldsymbol{\xi})$, for a spatial filter, designed to track the uniform displacement of the speckle pattern. Letting the image intensity define the relevant size of the spatial filter, we design a spatial filter with, e.g., a moderate selectivity with $N = 9$ unit cells ($2Mw_i = 9\Lambda_{x/y}$). The power spectrum is determined from Eq. (28), where the differential arrangement suppresses any even harmonics [16] in the photocurrent. As mentioned for Eq. (27), the power spectrum of the photocurrent $[P_i(\boldsymbol{\xi})]$ is defined as the product of the two spectra $[P_I(\boldsymbol{\xi})H(\boldsymbol{\xi})]$. Therefore, Fig. 4 illustrates how the fundamental frequencies ($\pm 1/\Lambda_{x/y}$) of the spatial filter have to coincide with a significant spatial frequency contribution within the speckle spectrum to ensure sufficient signal level. At the same time, the higher harmonics of the spatial filter should preferably be located beyond the spectral contents of the speckles to provide a sufficient suppression of their influence. As illustrated in Fig. 4, the second harmonic of the spatial filter is designed to coincide with the e^{-2} radius of the Gaussian speckle spectrum in order to suppress the higher harmonics. The corresponding criterion for the spatial filter can be written as

$$\Lambda_{x/y} = 3\sqrt{2}\frac{\lambda f_2}{\sigma}. \tag{29}$$

Figure 5 illustrates the power spectrum for a spatial filter designed for tracking the uniform displacement of the fringe patterns. The fringe spacing is the smallest structure; thus, the spatial filter is designed with a high selectivity ($N = 65$). In this case, the higher harmonics of this spatial filter are irrelevant for the filter response to fringes because the relative width of spectral contents of the fringe patterns is relatively narrow. The criterion for this spatial filter can be written as

$$\Lambda_z = \Lambda_{\mathrm{fr}} = \frac{\lambda}{|\varphi|}. \tag{30}$$

This behavior of speckles and fringes is numerically and experimentally documented in [8] in full agreement with Eq. (19d). Linear translations of an object in three dimensions, including directions, are measured by using two orthogonal spatial filters responding to the speckles and one spatial filter responding to the fringe patterns. The three velocity

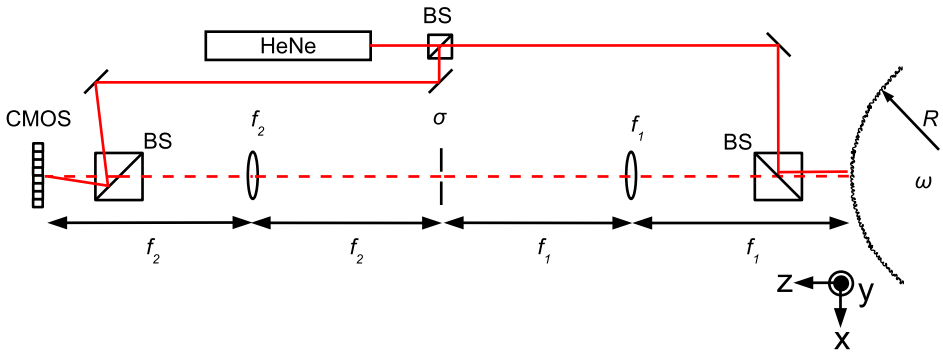

Fig. 7. (Color online) Schematic of the setup for obtaining the experimental data. HeNe, laser; BS, nonpolarizing beam splitters; f_1 and f_2, lenses of the imaging system; σ, circular aperture; CMOS, CMOS camera; R, radius of the object. The object rotates with an angular velocity of $\omega = \Delta\theta_x/\Delta t$.

components are measured with an uncertainty of less than $\pm 1\%$. Figure 4 illustrates that the fifth and seventh harmonics of the spatial filter, responding on the speckle patterns, do overlap with the spatial frequency band of the fringe patterns, and therefore cross talk from fringe motions could possibly contaminate the measurements of speckle motion. This is demonstrated numerically in [8], with a similar setup. However, as it is demonstrated, by choosing a $\varphi = (\varphi_x, \varphi_y)$ where $|\varphi_x| = |\varphi_y|$, a complete suppression of any cross talk between measurements on fringes and speckles is obtained.

In the case of measuring angular velocity [Eq. (22) or Eq. (24)], the fringe spacing is uniform throughout the observation plane and independent of angular velocity. However, the signal-phase shift ($\Delta\phi$) given a certain angular shift $\Delta\theta_x$ varies proportional to the position p_x of the filter in the observation plane. Even when addressing the two halves of the observation plane with two separate spatial filters, a spatial filter with a relatively large number (N) of unit cells will broaden the relative spectral width significantly and accordingly reduce the accuracy of this measurement. Instead, a small number of unit cells ($N = 1$–8) will optimize this specific measurement. In Fig. 6, the corresponding spatial power spectrum of a spatial filter is illustrated for $N = 3$. The criterion for this spatial filter is given in Eq. (30). Nevertheless, because the fringe intensity is a sinusoidal intensity distribution, even a single unit cell provides a quasi-sinusoidal photocurrent in response to a constant fringe velocity. Further, the differential measurement used in Eq. (22) to determine the angular shift $\Delta\theta_x$ independent of the center of rotation of the object will be carried out by two spatial filters that are separated by a distance d_p in the observation plane.

3. Experiments and Results

The setup is illustrated in Fig. 7. A linearly polarized He–Ne laser emits light at a wavelength of 633 nm. With a beam expander, the laser light is collimated to give a beam with a radius (e^{-2}) of approximately 1 mm and a confocal parameter of $2b = 10$ m. The expanded beam is split in two by a nonpolarizing beam splitter (BS). The first beam is directed toward the object to illuminate a region on its surface. The illuminated surface region is imaged onto the observation plane by a clean imaging system consisting of two lenses $f_1 = f_2 = 250$ mm ($|M| = 1.0$) and an adjustable aperture located in the focal plane shared by the two lenses. In the experiment, the amplitude transmission function of the aperture is a hard circular aperture with a radius of $\sigma = 0.75$ mm. For convenience the theory is based on a Gaussian aperture. Using a hard aperture will affect the spatial shape of the speckles [12] in the observation plane; thus, the theoretical and experimental speckle size will differ. However, the dynamics the speckle and fringes will not be altered by the shape of the aperture. The depth of focus of the given imaging system is approximately $d_o = 45$ mm. The second beam establishes the reference wave and is directed toward the observation plane, where it coincides with the image of the object under an angle of $\varphi = (0.0171\,\text{rad}, 0.0\,\text{rad})$ relative to the optical axis of the imaging system. The experiment obtains data from three cylindrical objects with radii of $R = 3.0$, 4.0, and 5.0 mm. The objects are made of aluminum, and their surfaces have a matte finish. Therefore, the object surfaces fulfill the assumption of Eq. (7) and produce fully developed speckles in the observation plane.

The objects are mounted on a rotational stage. The axes of symmetry of the cylindrical objects are adjusted to coincide with the axis of rotation of the rotational stage. Three different angular velocities have been calibrated for this experiment: $\Delta\theta_{x1}/\Delta t = 1.28 \times 10^{-3}$ rad/s, $\Delta\theta_{x2}/\Delta t = 1.89 \times 10^{-3}$ rad/s, and $\Delta\theta_{x3}/\Delta t = 2.49 \times 10^{-3}$ rad/s with a standard deviation of $\pm 0.5\%$. Note that the angular displacement of the object is parallel with the plane of incidence defined by the optical axis and reference beam. Therefore, the angular displacement of the object and the corresponding fringe displacement will vary in the p_x direction [Eq. (22)]). A complementary metal oxide semiconductor (CMOS) camera is located in the observation plane and has an array of $N_r \times N_c = 256 \times 256$ pixels with center spacings of $10.6\,\mu\text{m} \times 10.6\,\mu\text{m}$. The CMOS camera acquires 200–300 sequential images with a well-defined frame rate of 17.6 ± 0.1 frames/s, which provides an uncertainty

of less than 1%. Therefore, the images are acquired with angular differential steps of three different sizes: $\Delta\theta_{x1} = 7.26 \times 10^{-5}$ rad/frame, $\Delta\theta_{x2} = 1.07 \times 10^{-4}$ rad/frame, and $\Delta\theta_{x3} = 1.41 \times 10^{-4}$ rad/frame, dependent on the respective angular speed. Note that all the images are obtained during a total angular displacement of less than 1% of a revolution of the objects. The sequences of images are stored for later processing. The recording and postprocessing of images are designed into the experiment merely to simulate optical spatial filtering and demonstrate the principle of the proposed technique. As mentioned earlier, the proposed technique includes optical spatial-filtering velocimetry for real-time measuring of angular displacement or velocity.

During the postprocessing, the images are multiplied one by one, pixel by pixel with a set of masks that implements the required phase-stepped photocurrents of the spatial filter under consideration [10]. In the image obtained at a displacement of $\mathbf{s}$, the photocurrent $i_{s,r,c}$ is obtained due to light incident upon the pixel indexed by row r and column c. The mask contains a transmittance value $\alpha_{\phi,r,c}$ for each individual pixel in the image. During processing of an image sequence, the corresponding photocurrent $i_\phi(\mathbf{s})$ is determined as:

$$i_\phi(\mathbf{s}) = \sum_{c=1}^{N_u} \sum_{r=1}^{N_L} \alpha_{\phi,r,c} i_{\mathbf{s},r,c}. \tag{31}$$

Figure 8 illustrates a small fraction of a mask implementing a spatial filter with a rectangular-weighted, linear rectangular-array transmission function with its phase labeled by ϕ. A single unit cell is encapsulated by the thick black frame, and in this case the unit cell is implemented as a submask with an area of $N_u \times N_L$ pixels, where N_u and N_L simulate the different detectors in the unit cell and their common height, respectively. In this case, each column represents one detector; thus, $N_u = 4$. The unit cell is taken out of a linear array of N equivalent unit cells. The physical spacing between the unit cells is $\Lambda_m = N_u \times 10.6\,\mu$m, $w_m = 10.6\,\mu$m is the width of the individual rectangular elements in the unit cells, and $L_m = N_L \times 10.6\,\mu$m is the height of the unit cell. In the experiment, the number of unit cells and height of the unit cell will vary depending on the application. The individual transmittances are illustrated in Fig. 8. A second mask, which can produce the phase-shifted photocurrent $i_{\phi+\pi/2}(\mathbf{s})$, is implemented by shifting the transmittances of the first mask one column left or right.

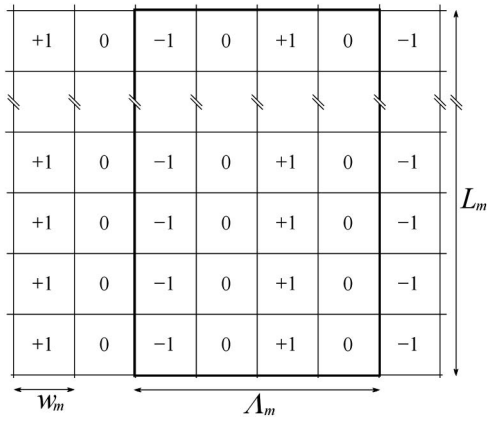

Fig. 8. A small fraction of the transmittance mask illustrates a unit cell, being a part of a spatial filter, producing the photocurrent $i_\phi(\mathbf{s})$ when processing a sequence of images. A second mask, which produces the photocurrent $i_{\phi+\pi/2}(\mathbf{s})$ in phase quadrature with $i_\phi(\mathbf{s})$, is equivalent to the first mask but shifted one column.

The two differential photocurrents, $i_1 = i_\phi(\mathbf{s})$ and $i_2 = i_{\phi+\pi/2}(\mathbf{s})$, introduced in Subsection 2.B, are produced directly with these masks. Because the frame rate of the camera is well defined, the two differential photocurrents are listed in the same chronological order as the corresponding images in order to produce sets of time records. Figure 9 illustrates a set of time records of the two photocurrents obtained with a sampling rate of 17.6 S/s. Clearly, the two photocurrents are two similar quasi-sinusoidal signals in mutual phase quadrature. The signal frequency (f_s) is determined by calculating the power spectra of the time records and finally applying a peak-finding algorithm to the power spectra. The signal frequency is

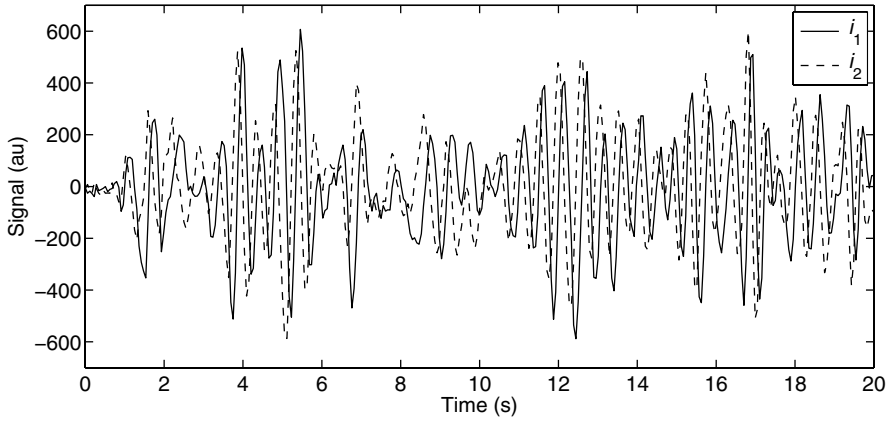

Fig. 9. The two time records illustrate the two constructed differential photocurrents, i_1 and i_2, as quasi-sinusoidal functions of time. The two photocurrents have a mutual phase lag of approximately $\pi/2$.

expected to be proportional to the horizontal position in the observation plane. Thus, the spatial average signal frequency measured by the spatial filter is assumed to represent the displacement at the center of the spatial filter. As the images progress with the maximum angular displacement rate of $\Delta\theta_{x3}$, the relative deviation in the fringe spacing due to the term $\Delta\theta_{x3}/(M\varphi_x)$ is predicted to be of the order of 1.0% of the fringe spacing at $\Delta\theta_x = 0$. Thus, we assume that the proportionality factor $[q_x/\Delta\phi = 1/(k\varphi_x))]$ between fringe displacement and signal-phase shift is independent of the angular displacement throughout these experiments.

The image in Fig. 10 illustrates the regular fringes and the random speckles obtained from the object with a radius of 5.0 mm. The speckle radius is $\rho = 95\,\mu$m, and the fringe spacing is estimated from a power spectrum of the image to be $\lambda_{\mathrm{fr}} = 37.0\,\mu$m; thus, the mean speckle contains $2\rho/\Lambda_{\mathrm{fr}} = 5.1$ fringes. This is approximately the same number of fringes per mean speckle as presented in Fig. 2. Thus, according to Figs. 4–6, the spectral contents of speckles and fringes are well separated, and any cross talk from the speckles dynamics in the fringe signal will be well suppressed. The angular displacement of the object per frame is of $\Delta\theta_{x1} = 7.26 \times 10^{-5}$ rad/frame. As discussed after Eqs. (20a) and (20b), an important limit was defined by the criterion of $R^2 \ll d_o^2$, where speckle boiling dominates any speckle translation in response of the peripheral velocity of the object. As $d_o = 45$ mm compared to $R = 5.0$ mm, the criterion indicates that Eqs. (20a) and (20b) are well within the limit, and accordingly we observe/measure no speckle translation in any of the image sequences. Therefore, in case we observe a translation of the speckles with an optical spatial filter, the measurement will contain no information about the angular displacement of the object.

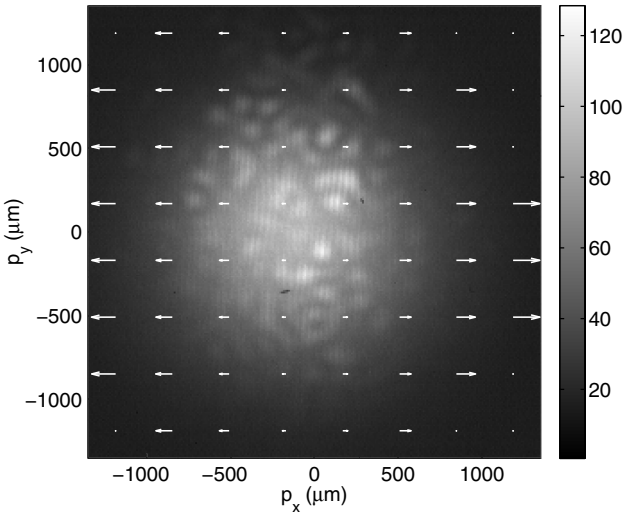

Fig. 10. Fringes and speckles overlaid with a vector map that illustrates the displacement rate (q_x) of the fringes as the object rotates about the y axis with an angular displacement of $\Delta\theta_{x1}$.

The displacement rate of the fringes throughout the observation plane is measured by probing the intensity in the observation plane with a spatial filter using the following parameters: $N = 8$ unit cells and $L_m = 32{\times}10.6\,\mu$m. Thus, the total area of the spatial filter is 32×32 pixels, and the filter is scanned by 8×8 steps in order to measure throughout the entire frame. As the center frequency of the spatial filter is specified by a pitch of the unit cells of $\Lambda_m = 4{\times}10.6\,\mu\mathrm{m} = 42.4\,\mu\mathrm{m}$ $(\neq\Lambda_{\mathrm{fr}})$, the spatial filter does not match the fringe spacing exactly. Unfortunately, the angle of incidence of the reference field was not correctly aligned during the experiments. Therefore, neither the signal level nor the mutual phase lag are optimized for the experiments. However, the levels of phase lag and signal are still sufficient for determining both the sign of the lag and demonstrating the principle of the proposed technology. The signal frequencies have been plotted as the corresponding fringe-displacement rates in a vector map, and the vector map has been printed superimposed on the image in Fig. 10. As we expect from Eq. (21), the local horizontal signal frequency $[f_{s,x}(p_x) = f_{s,x}(p_x, p_y)]$ for the spatial filter is proportional to the horizontal center position p_x of the spatial filter in the observation plane. Vertically, the signal frequency $[f_{s,y}(p_x, p_y)]$ is less than the measurement uncertainty at any position. Note that the center of rotation does not coincide exactly with the origin of the image. Further, the measurements in the corner of the vector map fail due to the lack of image intensity, as expected from the image-intensity-related correlation term in Eqs. (20a) and (20b).

The influence of the number of unit cells in the spatial filter when probing the local fringe displacement rate has been investigated for four different values: $N = 1, 2, 4$, and 8 unit cells. The height of the spatial filters is $L_m = 256{\times}10.6\,\mu$m, and the angular velocity of the object is $\Delta\theta_{x1}/\Delta t = 1.28 \times 10^{-3}$ rad/s. Clearly, by increasing the number of unit cells from $N = 1$ to $N = 2$, the selectivity of the filter increases, and the relative spectral width in the power spectra of the signal decreases. However, for $N > 2$ the relative spectral width increases due to the increasing range in the phase rates of the fringes as the physical extent of the spatial filter increases with the number of unit cells. Therefore, we select the spatial filter with $N = 2$ unit cells in the rest of this paper. As the gradient of the signal frequency with respect to the horizontal axis in the observation plane is constant, the spectral widths of the signals are independent of the horizontal position of the spatial filter (constant N). Therefore, the relative spectral width of the signals decreases with increasing horizontal position in the observation plane (assuming that $\Delta z = 0$). As mentioned above, the signal power drops with the image intensity as the distance to the center of the image increases. Therefore, a compromise between signal power and filter selectivity is of relevance when selecting the two optimum positions for a differential

measurement of angular velocity, according to Eq. (22).

The expected behavior of Eq. (21) can be quantized in more detail. Three image sequences are obtained for an object with a radius of $R = 4.0\,\text{mm}$ and rotating at the three calibrated angular velocities. With the spatial-filter parameters as selected above ($N = 2$, $L_m = 256{\times}10.6\,\mu\text{m}$), the spatial filter is scanned horizontally throughout the images. In Fig. 11 the signal-frequency measurements are plotted as the corresponding displacement rate of the fringes [$\Delta q_x/\Delta t = \Lambda_{\text{fr}} f_s$, Eq. (26)] versus the horizontal position of the spatial filter in the observation plane. In this way, the phase quadrature between i_1 and i_2 gives the direction of the fringe displacement rate. The theoretically obtained curves calculated from Eq. (21) are plotted as lines in Fig. 11.

Linear regression is applied to the signal-frequency measurements in Fig. 11 and provides the statistics listed in Table 1. The parameter c_1 is the first derivative of Eq. (26) with respect to p_x, and when adjusted by a factor of $M\varphi/2$ it provides a differential measurement of the angular velocity of the object—equivalent to Eq. (22). The corresponding deviations reflect systematic errors, which are apparent in Fig. 11. The column of $-c_0/c_1$ in Table 1 reflects the measured position of the image of the center of the rotation in the observation plane, assuming that the object is stationary along the axial direction, $\Delta z = 0$. The root-mean-square error (RMSE) indicates the spread of the data points around the trends provided by linear regression. The RMSE value is relative to the angular velocity at $p_x = 1.0\,\text{mm}$.

To verify that the fringe patterns move with respect to the angular velocity and not due to the peripheral surface velocity, three image sequences are recorded with the three objects, having different radii. All the objects rotate with an angular velocity of $\Delta\theta_{x1}/\Delta t = 1.28 \times 10^{-3}\,\text{rad/s}$, and the spatial-filter parameters are the same as used above, where $N = 2$ and $L_m = 256{\times}10.6\,\mu\text{m}$. In Fig. 12 we have plotted the difference between the measured angular velocities and the theoretical angular velocities [Eq. (21)] in order to see the deviations between the plots for the three different radii. The best fitted linear regression lines have been plotted as well, and their parameters and the statistics have been listed in Table 2.

The finite slopes of the linear regression lines for the angular velocity plots versus p_x are listed in the column $M\varphi c_1/2$ in Table 2 as angular velocities. Again, the slopes reflect the deviation between the measured and the expected values for the angular velocity, being approximately 1%. A correction to this value by 1% brings all the lines of linear regression close to being horizontal lines, separate vertically due to the individual offsets of the center of rotation of the three objects. Note that throughout the column of c_0/c_1^* in Table 2, the value for c_1^* is replaced with the value of c_1 determined for $\Delta\theta_x/\Delta t = 1.28\,\text{mrad/s}$

Table 1. Fitted Parameters of a Linear Regression Applied to Angular Velocities Estimated from the Measured Signal Frequencies Plotted in Fig. 11, Specified as $f_{s,x}^{\text{measured}} = c_0 + c_1 p_x$ [a]

Angular Velocity $\Delta\theta_x/\Delta t$ (mrad/s)	$-c_0/c_1$ (μm)	$M\varphi c_1/2$ (mrad/s)	R square	RMSE (% at $p_x = 1\,\text{mm}$)
1.28	−33.7	1.29	0.9999	0.71
1.89	−31.1	1.93	0.9998	1.15
2.49	−41.0	2.58	0.9999	0.67

[a]The RMSE value is relative to the angular velocity at $p_x = 1.0\,\text{mm}$.

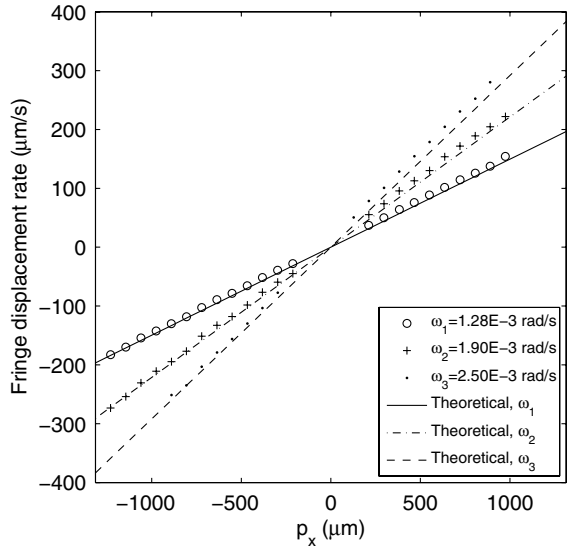

Fig. 11. The signal frequencies are plotted as the local fringe displacement rates versus the horizontal position of the spatial filter in the observation plane. The three calibrated angular velocities are addressed.

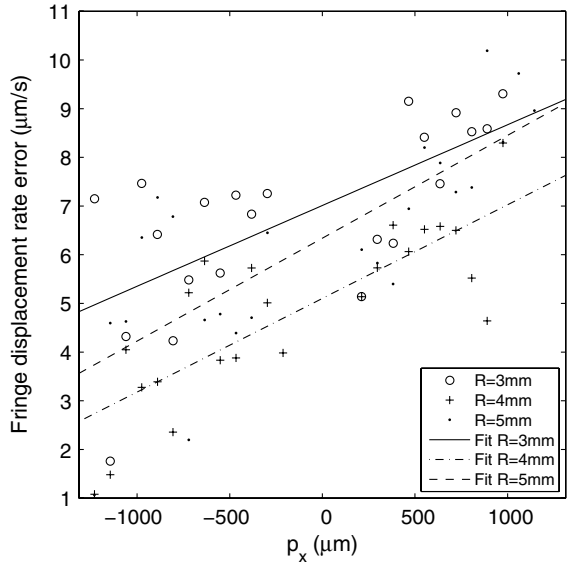

Fig. 12. The signal frequencies errors are plotted versus the horizontal position of the spatial filter in the observation plane. Three different object radii are addressed; $R = 3.0\,\text{mm}$, $R = 4.0\,\text{mm}$, and $R = 5.0\,\text{mm}$.

Table 2. Fitted Parameters of a Linear Regression Applied to the Measured Velocity Data Plotted Specified as $f_{s,x}^{\text{measured}} - f_{s,x}^{\text{theoretical}} = c_0 + c_1 p_x$ [a]

Radius of Curvature R (mm)	$-c_0/c_1^*$ (μm)	$M\varphi c_1/2$ (mrad/s)	R square	RMSE (% at $p_x = 1$ mm)
3	−46.2	1.42×10^{-2}	0.451	0.92
4	−33.7	1.64×10^{-2}	0.635	0.72
5	−41.8	1.81×10^{-2}	0.591	0.94

[a]The RMSE value is relative to the angular velocity at $p_x = 1.0$ mm.

in Table 1. The column lists the image position of the center of rotation for the three different objects.

4. Discussion and Conclusion

It has been demonstrated theoretically that, by combining speckle photography techniques with speckle interferometry in order to reveal the absolute phase of speckles by interference with a local oscillator (the reference wave), measurements of linear object movement in 3D can be obtained and conditioned for spatial-filtering velocimetry. The expectations are experimentally illustrated in [8], where the linear object motion in 3D is obtained with full directionality and, more importantly, any cross talk between measurements of fringes and speckle dynamics can be removed completely.

Second, the theoretical work indicates that, by investigating the dynamics of the optical structures in the observation plane locally, measurements of both out-of-plane rotation components can be obtained. In this work, measurements of angular velocity in the plane of object and reference beam incidence have been demonstrated to provide systematic errors within a few percent, and random errors within 1%.

It was observed experimentally that any effects of the peripheral motion of the surface on the speckle motions could be suppressed satisfactorily by letting the focal depth of the imaging system be substantially larger than the radius of the object ($R^2 \ll d_o^2$). This means that the speckle-decorrelation length is significantly shorter than any speckle translation obtained in the work here. In case of using a different design where the criterion is different (e.g., $R^2 \gg d_o^2$), the peripheral velocity will be directly measurable [18].

In case the experimental setup satisfies that $R^2 \ll d_o^2$, the technology cannot distinguish between measurements obtained from an object surface rotating with regard to an axis, being parallel with, e.g., the y axis but located at either $z = R$ or $z = -R$. For the same angular displacement, the fringe movements are indistinguishable in the two cases. However, in case $R^2 \gg d_o^2$, additional information from the speckle dynamics about the direction of the peripheral velocity could eliminate the ambiguity.

With knowledge of the position (p_{cr}) where the image of the center of rotation of the object is located in the observation plane, Eq. (25) reveals both the angular velocity $\Delta\theta_x$ and Δz (to be measured at $p_x = p_{\text{cr}}$) for the corresponding type of rotation. However, in case the center of object rotation is unknown, Δz must be determined by other means. The presence of a second reference beam with a different angle of incidence could be multiplexed with the original reference beam either in time or in space. In case the angles of incidence of the primary and secondary reference beams are $-\varphi$ and φ, respectively, the center of rotation will coincide in the measurements from both mixing options for $\Delta z = 0$. If $\Delta z \neq 0$, then Δz will introduce an equivalent magnitude of offset in the measurements but with a positive or negative sign when mixing with one or the other reference beam. Therefore, the position of the center of rotation of the object can be found using the symmetric influence of $\Delta z \neq 0$, and finally the correct Δz can be estimated.

In the experiments, the height of the spatial filter (L_m) is selected in order that the area ($N \times \Lambda_m \times L_m$) of the spatial filter always contains at least a few speckles. Naturally, the phases of the fringes encapsulated by the individual speckles are completely uncorrelated. Thus, in average, the amplitude of a differential photocurrent is raised by the square root of the number of speckles present within the spatial filter. At the same time the mean light intensity within the spatial filter is raised by the number of speckles; however, in principle, this contribution is eliminated in the differential photocurrent. The ability of the spatial filter to extract the fringe content from the image intensity is clearly illustrated in Fig. 9 despite a poor fringe visibility observed in Fig. 10. More details on optimizing a measurement of a photocurrent obtained from a photodetector that is illuminated with several speckles can be found in [19].

As mentioned earlier in the description of the spatial filter, a unit cell with three detectors [17] or pixels can produce the same two photocurrents as the unit cell suggested for this work. Therefore, the spatial filters implemented with the CMOS camera could have been a more compact, and, if needed, the limited bandwidth of the camera could have been used more efficiently. Accordingly, the speckle size could be reduced by increasing the radius of the aperture and allowing the system to collect the scattered light more efficiently.

Measurement of the orthogonal out-of-plane rotation will require a unit cell of similar Λ_m and orientation as the one used in the experimental work above. However, the height L_m of the unit cell should only be a fraction of the image height in order to avoid a severe spectral broadening of the signal. Instead, the number of unit cells can be increased to, e.g., extend the spatial filter across the entire image. However, increasing the size ($N\Lambda_m$) of the spatial filter beyond the speckle-decorrelation length provides no improvement in selectivity of the spatial filter. To perform differential measurements of the angular displacement $\Delta\theta_y$ or velocity $\Delta\theta_y/\Delta t$, the two spatial filters should be separated by the distance of d_p along the p_y axis, instead.

The possibility of measuring in-plane rotation is present as well and has been described thoroughly in [20]. As the object carries out an in-plane rotation with regard to a point in the object plane, similarly will the speckles rotate in the observation plane around a related point in the observation plane. The challenge will be to design the optimum geometry for the optical spatial filter.

The benefit of applying optical spatial-filtering velocimetry to the field of speckle interferometry is to obtain real-time measurements without time consuming correlation methods. In this work, a camera-based device has been used, but here merely in order to simulate the function of an optical spatial filter and demonstrate the viability of the technique. A complete implementation of speckle and fringe interpretation by optical spatial-filtering velocimetry is not within the scope of this work. Reference [8] demonstrates measurements of the axial component Δz with an optical spatial filter, though the processing of the data is still carried out with frequency analysis. In order to implement real-time processing, algorithms such as zero-crossing detection [21], zero-crossing rate detection [22,23], or phase unwrapping of two signals in phase quadrature [24] are required.

In conclusion, the proposed technique can measure motion in all 6 degrees of freedom. However, as discussed in [8], the decorrelation effects of the speckles will determine the limits and accuracy of the various combinations of measurements obtained from both speckles and fringes simultaneously.

This work has been funded partly by OPDI Technologies A/S.

References

1. A. E. Ennos, "Speckle Interferometry," in *Laser Speckle and Related Phenomenon*, J. C. Dainty, ed. (Springer-Verlag, 1984), pp. 203–253.
2. J. M. Burch and J. M. J. Tokarski, "Production of multiple beam fringes from photographic scatters," Opt. Acta **15**, 101–111 (1968).
3. M. Sjödahl, "Some recent advances in electronic speckle photography," Opt. Lasers Eng. **29**, 125–144 (1998).
4. I. Yamaguchi, "Fringe formation in deformation and vibration and measurements using laser light," in Vol. 22 of *Progress in Optics*, E. Wolf, ed. (Elsevier, 1985), pp. 272–340.
5. M. Sjödahl and H. O. Saldner, "Three-dimensional deformation field measurements with simultaneous TV holography and electronic speckle photography," Appl. Opt. **36**, 3645–3648 (1997).
6. T. Fricke-Begemann, "Three-dimensional deformation field measurement with digital speckle correlation," Appl. Opt. **42**, 6783–6796 (2003).
7. S. L. Yeh, S. T. Lin, and Y. H. Chang, "Precise displacement measurement for a local surface," Opt. Lett. **34**, 3406–3408 (2009).
8. T. F. Q. Iversen, M. L. Jakobsen, and S. G. Hanson, "Speckle-based three-dimensional velocity measurement using spatial filtering velocimetry," Appl. Opt. **50**, 1523–1533 (2011).
9. J. T. Ator, "Image velocity sensing by optical correlation," Appl. Opt. **5**, 1325–1331 (1966).
10. Y. Aizu and T. Asakura, *Spatial Filtering Velocitmetry: Fundamentals and Applications* (Springer-Verlag, 2006).
11. H. T. Yura and S. G. Hanson, "Optical beam wave propagation through complex optical systems," J. Opt. Soc. Am. A **4**, 1931–1948 (1987).
12. J. W. Goodman, *Speckle Phenomena in Optics: Theory and Applications* (Roberts, 2006).
13. H. T. Yura, B. Rose, and S. G. Hanson, "Dynamic laser speckle in complex *ABCD* optical systems," J. Opt. Soc. Am. A **15**, 1160–1166 (1998).
14. A. E. Siegman, *Lasers* (University Science, 1986).
15. S. Lowenthal and H. Arsenault, "Image formation for coherent diffuse objects: statistical properties," J. Opt. Soc. Am. **60**, 1478–1483 (1970).
16. U. Schnell, J. Piot, and R. Dändliker, "Detection of movement with laser speckle patterns: statistical properties," J. Opt. Soc. Am. A **15**, 207–216 (1998).
17. L. Mertz, "Complex interferometry," Appl. Opt. **22**, 1530–1534 (1983).
18. M. L. Jakobsen and S. G. Hanson, "Miniaturised optical sensors for industrial applications," Proc. SPIE **7726**, 77260P (2010).
19. M. Lehmann, "Phase-shifting speckle interferometry with unresolved speckles: a theoretical investigation," Opt. Commun. **128**, 325–340 (1996).
20. H. T. Yura, B. Rose, and S. G. Hanson, "Speckle dynamics from in-plane rotating diffuse objects in complex *ABCD* optical systems," J. Opt. Soc. Am. A **15**, 1167–1173 (1998).
21. N. Takai, T. Iwai, and T. Asakura, "Real time velocity measurements for a diffuse object using zero-crossing of laser speckle," J. Opt. Soc. Am. **70**, 450–455 (1980).
22. R. Barakat, "The level-crossing rate and above-level duration time of the intensity of a Gaussian random process," Inf. Sci. **20**, 83–87 (1980).
23. M. L. Jakobsen, F. Pedersen, and S. G. Hanson, "Zero-crossing detection algorithm for arrays of optical spatial filtering velocimetry sensors," Proc. SPIE **7003**, 70030T (2008).
24. M. L. Jakobsen, H. E. Larsen, and S. G. Hanson, "Optical spatial filtering velocimetry sensor for submicron, in-plane vibration measurements," J. Opt. A **7**, S303–S307 (2005).